for either $MVK^{V377I/+}$ or $MVK^{H20N/+}$). We have previously shown that protein prenylation is defective in PBMCs from this patient but not in either parent.[2] Stimulation with LPS and the NLRP3 activator nigericin elicited much greater IL-1β release in cells from the patient with MKD than from either parent, and this response was abolished by MCC950 (Fig 1, *J*).

Our observations clearly demonstrate that lack of prenylation in monocytic cells (using statin treatment, a pharmacologic model of MKD, or using authentic MKD cells from a patient) leads to enhanced formation of an NLRP3-dependent and pyrin-independent inflammasome upon LPS stimulation. Although loss of prenylation has been suggested to activate the pyrin inflammasome in mouse bone marrow–derived macrophages,[4,5] it is possible that defective prenylation promotes activity of distinct inflammasomes in different cell types. In monocytes, loss of protein prenylation caused by SIM treatment was alone insufficient for inducing NLRP3 inflammasome formation or caspase-1 activation (Fig 1, *B* and *C*) but substantially boosted LPS-induced inflammasome activity (speck formation, caspase-1 activation, IL-1β and IL-18 release, and pyroptosis) on stimulation with LPS (Fig 1, *B-D*, and see Fig E1, *C*). The underlying mechanism remains to be clarified but did not involve an enhancement of LPS-induced changes in mRNA levels (see Fig E2, *A*, in this article's Online Repository at www.jacionline.org) or changes in protein levels (see Fig E2, *B*) of pro–IL-1β, pro–IL-18, NLRP3, ASC, or pro–caspase-1. Enhanced inflammasome formation in prenylation-deficient THP-1 cells also occurred after stimulation with the TLR2 agonist Pam3CSK4 (Fig 1, *K*), which is consistent with the enhanced sensitivity of PBMCs from patients with MKD to both TLR2 and TLR4 agonists.[1]

These findings are of clinical relevance because they demonstrate that targeting the pyrin inflammasome in isolation might not be sufficient to resolve all the pathology associated with MKD. Rather, approaches to overcome the metabolic defect in the mevalonate pathway and restore normal protein prenylation could be more effective at preventing broader inflammasome activation.

We thank Professor Kirill Alexandrov and Dr Zakir Tnimov (University of Queensland) for providing reagents for the Rab prenylation assay and Dr Ryan Chai (Garvan Institute) and Dr Rebecca Coll (University of Queensland) for technical advice.

Oliver P. Skinner, BSc[a]
Julie Jurczyluk, BSc[a]
Paul J. Baker, PhD[b]
Seth L. Masters, PhD[b]
Alicia G. Rios Wilks, BSc[a]
Misaki S. Clearwater, BSc[a]
Avril A. B. Robertson, PhD, MChem, GCHEd[c]
Kate Schroder, PhD[d]
Sam Mehr, MBBS, BMedSci, FRCPA, FRACP[e]
Marcia A. Munoz, PhD[a]*
Michael J. Rogers, PhD[a]*

From [a]Bone Biology, Garvan Institute of Medical Research and St Vincent's Clinical School, UNSW Sydney, Sydney, Australia; [b]the Inflammation Division, Walter and Eliza Hall Institute of Medical Research, Melbourne, Australia; [c]the School of Chemistry and Molecular Biosciences and [d]the Institute for Molecular Bioscience, University of Queensland, Brisbane, Australia; and [e]the Department of Allergy/Immunology, Royal Children's Hospital, Melbourne, Australia. E-mail: m.rogers@garvan.org.au.

*These authors contributed equally to this work as senior authors.

Supported in part by NHMRC project grant APP1139644 (to M.J.R.), a grant from the Allergy and Immunology Foundation of Australasia (to M.A.M. and M.J.R.), Mrs Janice Gibson and the Ernest Heine Family Foundation, and the Marian & E.H. Flack Trust.

Disclosure of potential conflict of interest: A. A. B. Robertson and K. Schroder are co-inventors on patent applications for NLRP3 inhibitors, which have been licensed to Inflazome, a company headquartered in Dublin, Ireland. Inflazome is developing drugs that target the NLRP3 inflammasome to address unmet clinical needs in inflammatory disease. K. Schroder served on the Scientific Advisory Board of Inflazome in 2016-2017. The rest of the authors declare that they have no relevant conflicts of interest.

REFERENCES

1. Stoffels M, Jongekrijg J, Remijn T, Kok N, van der Meer JW, Simon A. TLR2/TLR4-dependent exaggerated cytokine production in hyperimmunoglobulinaemia D and periodic fever syndrome. Rheumatology (Oxford) 2015;54:363-8.
2. Munoz MA, Jurczyluk J, Mehr S, Chai RC, Arts RJW, Sheu A, et al. Defective protein prenylation is a diagnostic biomarker of mevalonate kinase deficiency. J Allergy Clin Immunol 2017;140:873-5.
3. Mandey SH, Kuijk LM, Frenkel J, Waterham HR. A role for geranylgeranylation in interleukin-1beta secretion. Arthritis Rheum 2006;54:3690-5.
4. Akula MK, Shi M, Jiang Z, Foster CE, Miao D, Li AS, et al. Control of the innate immune response by the mevalonate pathway. Nat Immunol 2016;17:922-9.
5. Park YH, Wood G, Kastner DL, Chae JJ. Pyrin inflammasome activation and RhoA signaling in the autoinflammatory diseases FMF and HIDS. Nat Immunol 2016;17:914-21.
6. Guo C, Chi Z, Jiang D, Xu T, Yu W, Wang Z, et al. Cholesterol homeostatic regulator SCAP-SREBP2 integrates NLRP3 inflammasome activation and cholesterol biosynthetic signaling in macrophages. Immunity 2018;49:842-56.e7.
7. Jurczyluk J, Munoz MA, Skinner OP, Chai RC, Ali N, Palendira U, et al. Mevalonate kinase deficiency leads to decreased prenylation of Rab GTPases. Immunol Cell Biol 2016;94:994-9.
8. Baker PJ, Boucher D, Bierschenk D, Tebartz C, Whitney PG, D'Silva DB, et al. NLRP3 inflammasome activation downstream of cytoplasmic LPS recognition by both caspase-4 and caspase-5. Eur J Immunol 2015;45:2918-26.
9. Coll RC, Robertson AA, Chae JJ, Higgins SC, Munoz-Planillo R, Inserra MC, et al. A small-molecule inhibitor of the NLRP3 inflammasome for the treatment of inflammatory diseases. Nat Med 2015;21:248-55.

Available online February 21, 2019.
http://dx.doi.org/10.1016/j.jaci.2019.02.013

F-BAR domain only protein 1 (FCHO1) deficiency is a novel cause of combined immune deficiency in human subjects

To the Editor:

Clathrin-mediated endocytosis (CME) is the major endocytic pathway by which eukaryotic cells internalize cell-surface cargo proteins and extracellular molecules, thereby enabling a broad range of biological processes, including cell signaling, nutrient and growth factor uptake, and cell fate and differentiation.[1] F-BAR domain only proteins 1 and 2 (FCHO1/FCHO2) are involved in the maturation of clathrin-coated pit formation.[2] Through the N-terminal F-BAR domain, they bind to phosphatidylinositol 4,5-biphosphate on the inner side of the cell membrane, inducing and stabilizing membrane curvature.[3] In addition, the FCHO1/FCHO2 C-terminal μ-homology domain mediates interaction with the epidermal growth factor receptor substrate 15 and cargo molecules.[3] Moreover, the linker region of FCHO1 acts as an allosteric activator of the adaptor protein 2 complex, enabling recruitment of clathrin to the assembling coat.[4,5]

Here we report 5 patients (P1-P5) from unrelated families of Italian (P1), Turkish (P2, P3, and P5) and Algerian (P4) origin (Fig 1, *A*) with biallelic *FCHO1* mutations and combined immunodeficiency, manifesting as recurrent and severe infections

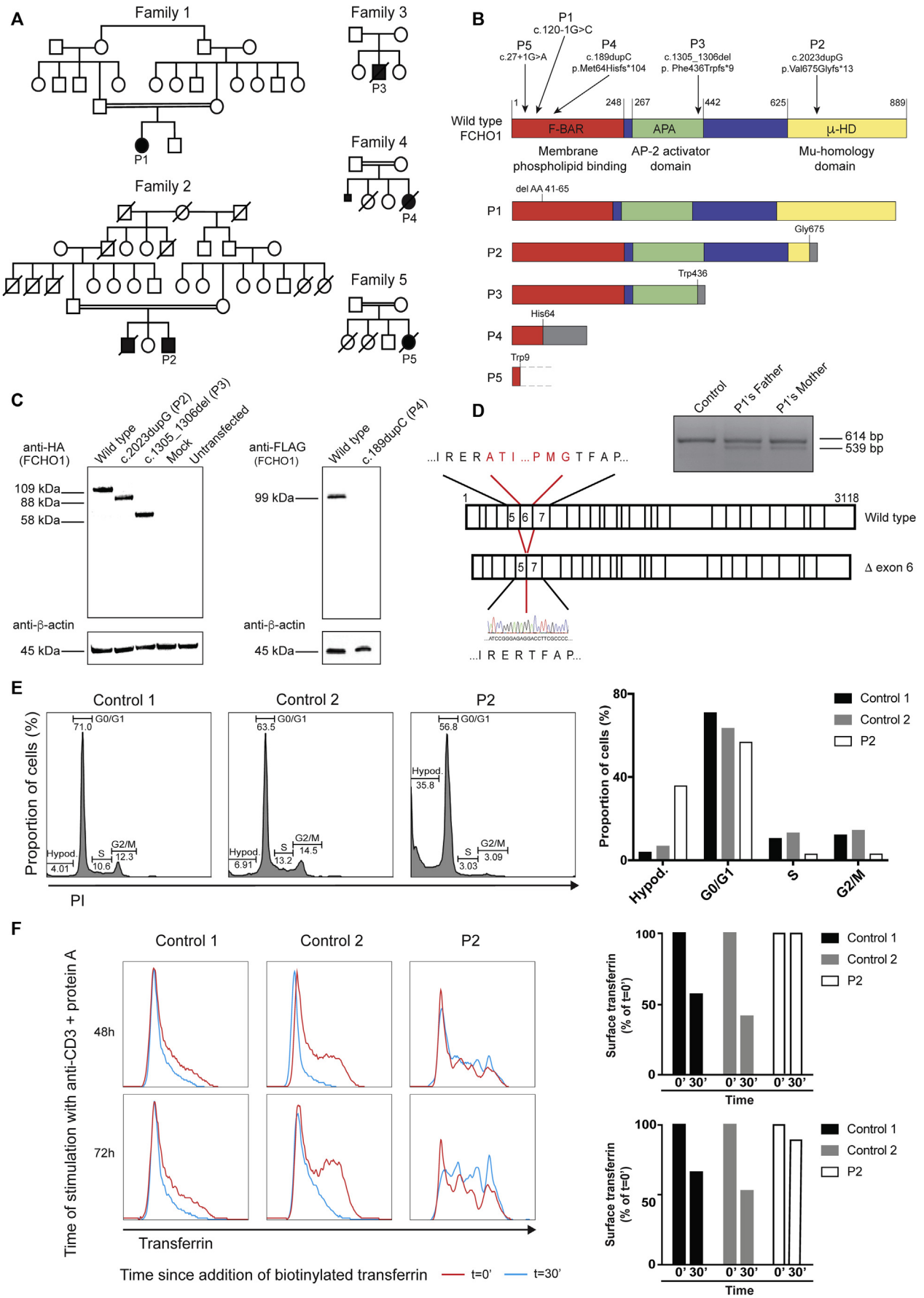

A
Family 1
P1
Family 2
P2
Family 3
P3
Family 4
P4
Family 5
P5
B
P1
c.120-1G>C
P5
c.27+1G>A
P4
c.189dupC
p.Met64Hisfs*104
P3
c.1305_1306del
p. Phe436Trpfs*9
P2
c.2023dupG
p.Val675Glyfs*13
Wild type
FCHO1
F-BAR
APA
μ-HD
Membrane
phospholipid binding
AP-2 activator
domain
Mu-homology
domain
del AA 41-65
Gly675
Trp436
His64
Trp9
C
anti-HA
(FCHO1)
Wild type
c.2023dupG (P2)
c.1305_1306del (P3)
Mock
Untransfected
109 kDa
88 kDa
58 kDa
anti-β-actin
45 kDa
anti-FLAG
(FCHO1)
Wild type
c.189dupC (P4)
99 kDa
anti-β-actin
45 kDa
D
Control
P1's Father
P1's Mother
614 bp
539 bp
...I R E R A T I ... P M G T F A P...
Wild type
Δ exon 6
...I R E R T F A P...
E
Control 1
Control 2
P2
Proportion of cells (%)
G0/G1
71.0
63.5
56.8
Hypod.
4.01
6.91
35.8
S
10.6
13.2
3.09
G2/M
12.3
14.5
PI
Control 1
Control 2
P2
F
Control 1
Control 2
P2
Time of stimulation with anti-CD3 + protein A
48h
72h
Transferrin
Time since addition of biotinylated transferrin
t=0'
t=30'
Surface transferrin
(% of t=0')
0' 30'
Time

TABLE I. Clinical and laboratory features of *FCHO1*-mutated patients

Clinical features	P1	P2	P3	P4	P5
Demographic					
Origin	Italian	Turkish	Turkish	Algerian	Turkish
Age at evaluation	3 y	18 mo	8 y	2.5 y	6 y
Infections					
Respiratory tract	Pneumonias, PJP, bronchiolitis	Pneumonias, bronchiolitis	Pneumonias	Pneumonias	Pneumonias
Gastrointestinal tract	Chronic diarrhea	Chronic diarrhea	—	Colitis	—
Others	Disseminated *Mycobacterium genavense* infection	—	Varicella, EBV viremia	Skin abscess, dermatophytosis	EBV viremia, fungal pneumonia
Growth failure	+	+	—	—	+
Lymphoproliferation					
Splenomegaly	+	—	+	+	—
Lymphadenopathy	+	—	+	+	—
Malignancies	—	—	EBV-negative DLBCL	—	—
Outcome	Alive with growth failure 13.8 y after HSCT	Alive and well 2.5 y after HSCT	Deceased	Deceased	Deceased
Laboratory data					
ALC (cells/μL)	**700**	**1000**	**542**	**1159**	**1200**
ANC (cells/μL)	7940	3100	5650	4575	3570
$CD3^+$ (cells/μL)	**6**	**360**	**184**	**823**	**792**
$CD4^+$ (cells/μL)	**2**	**245**	**27**	**100**	**95**
$CD8^+$ (cells/μL)	**2**	**82**	**108**	**206**	**308**
$CD19^+$ (cells/μL)	459	180	**65**	220	120
$CD16/CD56^+$ (cells/μL)	192	320	103	116	120
IgG (mg/dL)	470 (on IVIG)	460	2230	833	909
IgA (mg/dL)	24	26	109	**9**	112
IgM (mg/dL)	45	**30**	173	**29**	428

ALC, Absolute lymphocyte count; *ANC*, absolute neutrophil count; *DLBCL*, diffuse large B-cell lymphoma; *GI*, gastrointestinal; *IVIG*, intravenous immunoglobulins; *PJP*, *Pneumocystis jirovecii* pneumonia. Abnormal values are shown in boldface.

of bacterial, mycobacterial, viral, and fungal origin and profound T-cell lymphopenia (Table I and see Fig E1 and the Methods section in this article's Online Repository at www.jacionline.org). P3 had EBV-negative diffuse large B-cell lymphoma. Three patients (P3-P5) died in childhood, whereas P1 and P2 are alive with full donor chimerism after allogeneic hematopoietic stem cell transplantation (HSCT) and have cleared pretransplantation infections. Whole-exome sequencing (P1, P2, P4, and P5) and targeted sequencing of a large panel of primary immune deficiency–related genes (P3) identified biallelic private *FCHO1* mutations, which were subsequently confirmed by means of Sanger sequencing (Fig 1, *B*, and see Fig E2, Table E1, and the Methods section in this article's Online Repository at www.jacionline.org).

Patients P2, P3, and P4 carried homozygous frameshift mutations predicted to cause premature termination. Western blotting analysis of HA- or FLAG-tagged *FCHO1* constructs showed expression of truncated products corresponding to P2 and P3, whereas no protein was detected for P4 (Fig 1, *C*).

P1 was homozygous for a splice-site mutation (c.120-1G>C) at the acceptor splice site of intron 5, which was predicted to result in exon 6 skipping. Because no pre-HSCT specimens were available, we performed RT-PCR analysis in PBMCs from her parents, who are both heterozygous for the mutation. Amplification with primers in exons 4 and 9 identified 2 bands in P1's parents; cloning and sequencing confirmed that the lower band corresponds to a product lacking exon 6 (Fig 1, *D*). This

FIG 1. A, Pedigrees of patients (P1-P5) with *FCHO1* mutations. **B,** Schematic representation of FCHO1 protein and predicted effects of mutations on protein structure. *Gray boxes* represent spurious amino acid sequences downstream of frameshift mutations. *Dashed lines* in P5 indicate undefined effects of the splice-site mutation downstream of Trp9. *AP-2*, Adaptor protein 2; *μHD*, μ-homology domain. **C,** Western blot of protein lysates from 293T cell lines transfected with plasmids encoding HA-tagged (P2 and P3) or FLAG-tagged (P4) WT or mutant *FCHO1* cDNA. β-Actin served as a protein-loading control. **D,** *Top*, RT-PCR amplification of partial (exons 4-9) *FCHO1* transcript in PBMCs from a healthy control subject and from P1's father and mother. *Bottom*, Schematic representation of effects at the transcript level, as predicted on cloning and sequencing of the 614-bp *(top)* and 539-bp *(bottom)* products, respectively. **E,** *Left*, Fluorescence-activated cell sorting *(FACS)*–based cell-cycle analysis on T-cell activation through CD3 and CD28 for 72 hours in P2 and 2 healthy control subjects. Staining with propidium iodide *(PI)* marks hypodiploid *(hypod.)* cells, as well as cells in the G0/G1, S, and G2/M phases of the cell cycle. *Right*, Proportion of PBMCs that were hypodiploid or in various phases of the cell cycle. **F,** *Left*, FACS analysis of the kinetics (t = 0 and 30 minutes) of transferrin internalization in T cells from 2 healthy control subjects and P2 on stimulation with anti-CD3 plus Protein A for 48 hours *(top)* and 72 hours *(bottom)*. *Right*, Graphic representation of biotinylated transferrin present on the cell surface at time point t = 30 minutes relative to t = 0 minutes.

abnormal splicing is predicted to cause an in-frame, internally truncated FCHO1 protein lacking amino acids 41 to 65 within the F-BAR domain (Fig 1, *B*).

P5 was homozygous for the c.27+1G>A mutation, which was predicted to disrupt the intron 2 donor splice site and the correct FCHO1 amino acid sequence after Trp9 (Fig 1, *B*). No samples were available to test the consequences of this mutation at the cDNA level.

We performed quantitative PCR analysis of *FCHO1* and *FCHO2* expression in control $CD4^+$ and $CD8^+$ T cells, $CD19^+$ B cells, $CD56^+$ natural killer cells, fibroblasts, and the K562 erythroleukemic cell line and observed differential expression. *FCHO1* was predominantly expressed in lymphoid cells, whereas *FCHO2* was more abundantly expressed in fibroblasts and K562 cells (see Fig E3 in this article's Online Repository at www.jacionline.org).

To clarify the mechanisms underlying the T-cell lymphopenia observed in the patients, we first analyzed T-cell activation and proliferation in PBMCs from healthy control subjects and P2, the only patient from whom pre-HSCT PBMCs were available. T cells from P2 displayed normal expression of early and late T-cell activation markers (CD69, CD25, and CD71) but reduced proliferation on activation through CD3/CD28 (see Fig E4, *A* and *B*, in this article's Online Repository at www.jacionline.org). In particular, T cells from P2 entered only 2 to 4 rounds of cell division, whereas T cells from control subjects entered 5 to 7 rounds of proliferation. Because each round of division that fails to occur in the patient results in an exponential loss in T-cell numbers,[6] the reduced number of cell divisions observed in P2 represents a significant proliferation defect. Prior studies have demonstrated that clathrin-mediated endocytosis is important for mitosis.[7] We found that after activation through CD3/CD28, PBMCs from P2 showed a high percentage of hypodiploid cells, a marker of apoptosis, and reduced percentages of cells in the S and G2/M phases of the cell cycle (Fig 1, *E*). Notably, no abnormalities of T-cell repertoire diversity, composition, and clonal abundance were observed in circulating T cells from P2 (see Fig E5 in this article's Online Repository at www.jacionline.org). Overall, these results strongly suggest that defective T-cell proliferation and increased activation-induced cell death, rather than impaired thymic output, are major contributors to the T-cell lymphopenia observed in patients with FCHO1 deficiency.

Finally, to investigate whether *FCHO1* mutations affect CME, we analyzed transferrin internalization, which relies mainly on clathrin-dependent endocytosis. We previously demonstrated that a missense mutation in *TFRC,* which encodes the transferrin receptor (TfR), impairs transferrin internalization and intracellular iron delivery, causing a combined immunodeficiency with defective T-cell proliferation.[8] TfR expression on the surfaces of resting PBMCs is minimal but increases at 48 and 72 hours after T-cell receptor (TCR) activation.[8] Therefore we stimulated PBMCs from P2 and control subjects with anti-CD3 and Protein A for 48 and 72 hours. A chase experiment was then performed by adding biotinylated transferrin, followed by streptavidin–phycoerythrin (PE), to measure the amount of biotinylated transferrin remaining on the cell surface after 30 minutes. Although transferrin internalization was readily observed in control T cells, it was minimally detectable in P2's T cells (Fig 1, *F*), which is consistent with previous observations that disruption of the *FCHO1* and *FCHO2* genes significantly affects the rate of TfR internalization but does not completely abrogate it.[5] Along with the different degree of impairment of T-cell proliferation, these findings distinguish FCHO1 deficiency from *TFRC* deficiency. In contrast, TCR/CD3 internalization, which is clathrin independent,[9] was preserved in activated T cells from P2 (see Fig E4, *C*).

In summary, we have demonstrated that FCHO1 deficiency is a novel form of combined immunodeficiency with impaired T-cell proliferation, increased activation-induced T-cell death, and defective CME.

We thank the Regeneron Genetics Center for DNA sequencing and bioinformatics support leading to the identification of the mutation in Family 2.

Enrica Calzoni, MD[a,b]*
Craig D. Platt, MD, PhD[c]*
Sevgi Keles, MD[d]
Hye Sun Kuehn, PhD[e]
Sarah Beaussant-Cohen, MD[c]
Yu Zhang, PhD[a]
Julia Pazmandi, MSc[f]
Gaetana Lanzi, PhD[b]
Francesca Pala, PhD[a]
Azzeddine Tahiat, PhD[g,h]
Hasibe Artac, MD[i]
Raul Jimenez Heredia, MSc[f]
Jasmin Dmytrus, MSc[f]
Ismail Reisli, MD[d]
Vedat Uygun, MD[j]
Dilara Uygun, MD[k]
Aysen Bingol, MD[k]
Erdem Basaran, MD[l]
Kamel Djenouhat, MD, PhD[g,h]
Nafissa Benhalla, MD, PhD[m]
Chafa Bendahmane, MD[n]
Melike Emiroglu, MD[o]
Tomas Kirchhausen, PhD[p]
Mithun Pasham, MS[p]
Jennifer Jones, BA[c]
Jacqueline G. Wallace, BSPH[c]
Lixin Zheng, MD[q]
Bertrand Boisson, PhD[r,s,t]
Fulvio Porta, MD[u]
Sergio D. Rosenzweig, MD, PhD[e]
Helen Su, MD, PhD[a]
Silvia Giliani, PhD[b]
Michael Lenardo, MD[q]
Raif S. Geha, MD[c]
Kaan Boztug, MD[f,v,w,x]
Janet Chou, MD[c]‡
Luigi D. Notarangelo, MD[a]‡

From [a]the Laboratory of Clinical Immunology and Microbiology and [q]the Laboratory of Immunology, National Institute of Allergy and Infectious Diseases, National Institutes of Health, Bethesda, Md; [b]"A. Nocivelli Institute for Molecular Medicine", Department of Molecular and Translational Medicine, University of Brescia, Brescia, Italy; [c]the Division of Immunology, Boston Children's Hospital, Harvard Medical School, Boston, Mass; [d]the Division of Pediatric Immunology and Allergy, Meram Medical Faculty, Necmettin Erbakan University, Konya, Turkey; [e]the Immunology Service, Department of Laboratory Medicine, Clinical Center, National Institutes of Health, Bethesda, Md; [f]the Ludwig Boltzmann Institute for Rare and Undiagnosed Diseases, Vienna, Austria; [g]the Laboratory of Medical Biology, Rouiba Hospital, Algiers, Algeria; [h]the Algiers Faculty of Medicine, University of Algiers 1, Algiers, Algeria; [i]Pediatric Immunology and Allergy and [o]Pediatric Infectious Diseases, Selcuk University Medical Faculty, Konya, Turkey; [j]Medical Park, Antalya Hospital, Pediatric Bone Marrow Transplantation Unit, Antalya, Turkey; [k]the Department of Immunology-Allergy and [l]the Department of Pediatric Pulmonology, Akdeniz University School of Medicine, Antalya, Turkey; [m]the Department of Pediatrics,

Beni Messous University Hospital, Algiers, Algeria; [n]the Department of Pediatrics, Meftah Hospital, Blida, Algeria; [p]the Department of Cell Biology, Harvard Medical School, and Program in Cellular and Molecular Medicine, Boston Children's Hospital, Boston, Mass; [r]St Giles Laboratory of Human Genetics of Infectious Diseases, Rockefeller Branch, Rockefeller University, New York, NY; [s]the Laboratory of Human Genetics of Infectious Diseases, Necker Branch, INSERM U1163, Necker Hospital for Sick Children, Paris, France; [t]Imagine Institute, Paris Descartes University, Paris, France; [u]Pediatric Onco-Haematology and BMT Unit, Children's Hospital, ASST Spedali Civili of Brescia, Brescia, Italy; [v]CeMM Research Centre for Molecular Medicine of the Austrian Academy of Sciences, Vienna, Austria; and [w]the Department of Pediatrics and Adolescent Medicine and [x]St Anna Children's Hospital and Children's Cancer Research Institute, Department of Pediatrics, Medical University of Vienna, Vienna, Austria. E-mail: janet.chou@childrens.harvard.edu. Or: luigi.notarangelo2@nih.gov.

*These authors contributed equally to this work.

‡These authors contributed equally to this work.

Supported by the Division of Intramural Research,National Institute of Allergy and Infectious Diseases, National Institutes of Health, Bethesda, Maryland, and by the "Angelo Nocivelli" Foundation.

Disclosure of potential conflict of interest: The authors declare that they have no relevant conflicts of interest.

REFERENCES

1. Kaksonen M, Roux A. Mechanisms of clathrin-mediated endocytosis. Nat Rev Mol Cell Biol 2018;19:313-26.
2. Cocucci E, Aguet F, Boulant S, Kirchhausen T. The first five seconds in the life of a clathrin-coated pit. Cell 2012;150:495-507.
3. Henne WM, Boucrot E, Meinecke M, Evergren E, Vallis Y, Mittal R, et al. FCHo proteins are nucleators of clathrin-mediated endocytosis. Science 2010; 328:1281-4.
4. Hollopeter G, Lange JJ, Zhang Y, Vu TN, Gu M, Ailion M, et al. The membrane-associated proteins FCHo and SGIP are allosteric activators of the AP2 clathrin adaptor complex. Elife 2014;3.
5. Umasankar PK, Ma L, Thieman JR, Jha A, Doray B, Watkins SC, et al. A clathrin coat assembly role for the muniscin protein central linker revealed by TALEN-mediated gene editing. Elife 2014;3.
6. Marchingo JM, Kan A, Sutherland RM, Duffy KR, Wellard CJ, Belz GT, et al. Antigen affinity, costimulation, and cytokine inputs sum linearly to amplify T cell expansion. Science 2014;346:1123-7.
7. Boucrot E, Kirchhausen T. Endosomal recycling controls plasma membrane area during mitosis. Proc Natl Acad Sci USA 2007;104:7939-44.
8. Jabara HH, Boyden SE, Chou J, Ramesh N, Massaad MJ, Benson H, et al. A missense mutation in TFRC, encoding transferrin receptor 1, causes combined immunodeficiency. Nat Genet 2016;48:74-8.
9. Compeer EB, Kraus F, Ecker M, Redpath G, Amiezer M, Rother N, et al. A mobile endocytic network connects clathrin-independent receptor endocytosis to recycling and promotes T cell activation. Nat Commun 2018;9:1597.

Available online February 26, 2019.
http://dx.doi.org/10.1016/j.jaci.2019.02.014

Gene expression signatures of circulating human type 1, 2, and 3 innate lymphoid cells



To the Editor:

Innate lymphoid cells (ILCs) are a functionally and phenotypically heterologous group of small lymphocytes that lack conventional linage markers but can become potent effector cells upon appropriate stimulations thereby producing large amounts of cytokines. Some examples of ILCs include natural killer (NK) cells, lymphoid tissue-inducer cells, and helper-like ILCs. This study focuses on the helper-like ILCs.

Helper-like ILCs are currently divided into 3 different subsets according to their distinct patterns of cytokine production and master transcription factors, which resemble helper T-cell subsets. In general, type 1 innate lymphoid cells (ILC1s) resemble T_H1 cells and have been implicated in immunity against intracellular pathogens, type 2 innate lymphoid cells (ILC2s) resemble T_H2 cells and have been implicated in immunity against helminths, and type 3 innate lymphoid cells (ILC3s) resemble T_H17 and T_H22 cells and have been implicated in immunity against extracellular bacteria. Interestingly, unlike T-helper subsets, recent studies revealed that ILCs are highly plastic cells that enable them to respond promptly to environmental changes.[1] In addition to being functionally diverse and interconvertible, the developmental pathways of ILCs are not well understood. Although gene expression profiles of ILCs have been studied in tissues, such as human tonsils,[2] only limited information is available on human circulating ILCs.[3] Tissue-resident ILCs could be quite different from the ILCs in blood. To understand the distinct functions of the type 1, 2 and 3 ILC subsets, it is necessary to delineate both the overlapping and unique functional signatures of these cells.

We present here one of the first whole-genome gene expression studies of the 3 ILC subsets from peripheral blood of healthy donors. The study was approved by the Cantonal Ethics Committee of Zurich. This study aims to establish the human ILC transcriptome reference data set in healthy subjects for comparison in disease settings, with enhanced utility because in most clinical situations blood samples but not tissue biopsy specimens are readily available.

A robust "2-round sorting" procedure was used to obtain highly pure ILC subsets. In brief, ILC subsets were isolated by using flow cytometry according to a published protocol by the Mjösberg group[2] with minor modifications: ILC1s as $CD45^+Lin^-CD127^+CD161^+CRTH2^-c\text{-}Kit^-$, ILC2s as $CD45^+Lin^-CD127^+CD161^+CRTH2^+c\text{-}Kit^-$, and ILC3s as $CD45^+Lin^-CD127^+CD161^+CRTH2^-c\text{-}Kit^+$. The purity of ILCs during this first-round sort was approximately 90% for ILC1s, 94% for ILC2s, and 58% for ILC3s. The ILCs were then resorted, collecting 1000 cells per subset by using more stringent gating directly into lysis buffer. Additional sorting experiments confirmed that the final ILC purity was high (86% to 96%), and more importantly, there was no detectable contamination of lineage-positive cells after second sorting (see Fig E1 in this article's Online Repository at www.jacionline.org). The samples (3 ILC subsets per donor and 6 different male healthy donors aged 25–40 years; ie, 18 samples in total) were analyzed by using RNA sequencing (RNAseq; raw data are available at the Gene Expression Omnibus as GSE112591, token yhmbgicchdkbncv).

A total of 13,297 genes were detected as being expressed. Principal component analysis revealed 3 clearly distinct clusters of each ILC subset (Fig 1, *A*), demonstrating significantly distinct gene expression profiles of ILCs.

The key ILC gene signatures were expressed as expected, such as high *IL7R* and *KLRB1* expression (encoding CD127 and CD161, respectively) in all ILC subsets, high *PTGDR2* (encoding CRTH2) and *GATA3* (encoding GATA-binding factor 3) expression in ILC2s, high *KIT* (encoding c-Kit) and *AHR* (encoding Aryl hydrocarbon receptor) expression in ILC3s, and high *EOMES* (encoding eomesodermin homolog) expression in ILC1s (Fig 1, *B*). This provides validation of the cellular identity for each ILC subset and demonstrates the effectiveness of our sorting strategy. *NCR2* (encoding NKp44) is detected at low levels across all samples, which is not surprising given that we sorted for $NKp44^-$ ILC3s.

First, we examined the top 200 most abundantly expressed genes in each ILC subset. Fig 1, *C*, provides a Venn diagram of these genes, which are 246 in total, with 194 differentially

METHODS

Patients

All study participants were recruited after obtaining informed consent, and the study was approved by the institutional review board of the referring institutions (National Institutes of Health protocols 06-I-0015 and 16-I-N139).

P1, of Italian origin, was born to first-cousin parents (Fig 1, *A*) and manifested recurrent respiratory and gastrointestinal tract infections since the first months of life. At the age of 3 years, she was admitted for *Pneumocystis jirovecii* pneumonia, diarrhea, and growth failure (weight, 12.9 kg, less than the third percentile; length, 97 cm, less than the third percentile). Laboratory examinations revealed profound lymphopenia (Table I). An abdominal computed tomographic (CT) scan showed diffuse mesenteric lymphadenopathy, and a lymph node biopsy specimen grew *Mycobacterium genavense*. At the age of 3 years and 7 months, the patient received a matched unrelated donor hematopoietic cell transplantation with myeloablative conditioning. The clinical course after transplantation was complicated by chronic graft-versus-host disease, autoimmune hemolytic anemia, and portal hypertension. She is currently alive at 17 years of age, with multilineage full donor chimerism. Her mycobacterial disease has resolved, but because of intestinal chronic graft-versus-host disease, she remains with low weight (35.9 kg) and height (128 cm).

P2, a boy born to consanguineous parents of Turkish origin (Fig 1, *A*), had recurrent respiratory tract infections and growth failure (weight, 7.8 kg, les than the third percentile) since 6 months of age. Laboratory investigations revealed T-cell lymphopenia, decreased serum IgM levels, and poor antibody responses (Table I). No thymic shadow was visible at chest radiography, and a chest CT scan demonstrated diffuse bronchiectasis (Fig E1, *A*). He was initially treated with intravenous immunoglobulin and antimicrobial prophylaxis and received a matched unrelated donor hematopoietic cell transplantation with myeloablative conditioning at the age of 2.5 years. The posttransplantation course was complicated by engraftment syndrome, which was successfully treated with steroids, and grade II acute graft-versus-host disease. He is currently alive and well, with full donor chimerism at 4 years of age.

His older brother was admitted at 1 year of age with a history recurrent pneumonias, diarrhea, candidiasis, and growth failure (weight, 5 kg, less than the third percentile) since the age of 7 months. Laboratory tests revealed T- and B-cell lymphopenia, hypogammaglobulinemia, and impaired antibody responses, for which he was treated with intravenous immunoglobulin. At the age of 6 years, he had severe pneumonia, *Candida* species–related sepsis, and vesicular lesions on his back. Despite extensive antibacterial and antifungal therapy, he developed multiorgan failure and died.

P3, a male child born to apparently nonconsanguineous parents from the same small village in Turkey, was admitted at the age of 8 years because of fever and dyspnea. Ultrasound studies revealed diffuse lymphadenopathy, and high levels of EBV viremia (178,000 copies/mL) were demonstrated. During follow-up, both lymphopenia and neutropenia were observed (Table I); a bone marrow biopsy specimen was consistent with hemophagocytic lymphohistiocytosis. Because of persistent lymphadenopathy, a lymph node biopsy was performed and revealed a diffuse EBV-negative large B-cell lymphoma. His clinical course was complicated by respiratory failure, leading to death.

P4, a female child born to consanguineous parents of Algerian origin, had an older sister with a history of disseminated BCG, chronic diarrhea, and recurrent pneumonias who died from a severe pneumonia resulting in acute respiratory failure. P4 had recurrent pneumonias, chronic diarrhea, skin abscesses, and refractory dermatophytosis at 4 months of age. By 2.5 years of life, she experienced neuromotor regression, with an inability to stand or sit, ataxia, hypermetria, and tremors. Immunologic evaluation at 2.5 years of life was notable for $CD4^+$ and $CD8^+$ lymphopenia, reduced IgM and IgA levels, reduced B-cell numbers, and nearly absent memory B cells. She continued to have recurrent pneumonias and died at 4 years of age of respiratory failure.

P5, a female child born to first-cousin parents of Turkish origin, was admitted at 6 years of age with fever, dyspnea, oral thrush, new-onset ataxia and seizures. She had no history of prior recurrent infections. Chest and abdominal CT revealed bilateral areas of consolidation and nodular opacities, as well as hepatic lesions that were identified as granulomas on histologic analysis. Cultures of bronchoalveolar lavage fluid were positive for *Klebsiella pneumoniae*. Brain magnetic resonance imaging revealed multiple 1.5-cm nodules in the right cerebellar hemisphere. Laboratory testing at that time was notable for $CD4^+$ T-cell lymphopenia, increased IgM levels, and EBV viremia (38,000 copies/mL). During this hospitalization, she had worsening respiratory failure accompanied by increasing size of cerebellar lesions despite treatment with meropenem, vancomycin, metronidazole, acyclovir, and amphotericin B. Histologic analysis of the brain lesions revealed angiocentric and angiodestructive lymphoid infiltrate admixed with histiocytes, with atypical $CD20^+$ lymphoid cells positive for EBV and CD30, which is consistent with a diagnosis of lymphomatoid granulomatosis. She was treated with rituximab and prednisone but died of respiratory failure.

Whole-exome sequencing, targeted sequencing, and Sanger DNA sequencing

For P1 and P2, genomic DNA samples were isolated from PBMCs by using the DNeasy Blood & Tissue Kit (69506; Qiagen, Hilden, Germany). After quality control, whole-exome sequencing (WES) for family 1 was performed with the VCRome 2.1 capture kit from NimbleGen and sequenced as paired-end 75-bp reads with the Illumina HiSeq 2500 Platform (Illumina, San Diego, Calif). For family 2, WES was performed with the Agilent Human V5 (51MB) Kit (Agilent Technologies, Waghäusel-Wiesental, Germany) coupled with paired-end 125-bp reads by using HiSeq 2500. All DNA samples were sequenced so that more than 85% of the bases were covered at 20× or greater. All sequenced DNA reads were mapped to the hg19 human genome reference by using the Burrows-Wheeler Aligner with default parameters. Single nucleotide variant and indel calling were performed by using the Genome Analysis Toolkit (version 3.4; the Broad Institute, http://www.broadinstitute.org/gatk/).

Variants were then annotated by using VEP and filtered by using GEMINI[E1] based on autosomal recessive mode of inheritance, a minor allele frequency of less than 0.01 in the ExAC browser, and the nonsynonymous nature of variants falling in coding regions or in splice sites. Blacklisted[E2] nonpathogenic common variants were also filtered out. Variant conservation and functional prediction, gene expression pattern, and available known biological knowledge were used to prioritize the candidate variants to identify the disease causal variant from rare family private variants.

For P3, genomic DNA was enriched with the HaloPlex Target Enrichment System (Agilent Technologies), and targeted sequencing of 500 primary immune deficiency genes and data analysis were performed, as previously described.[E3]

For patients P4 and P5, genomic DNA was isolated from whole blood by using the Gentera Puregene Cell Kit (Qiagen). Exome capture was performed by using the Agilent SureSelect V5, 51MB (Agilent Technologies). The Illumina HiSeq-2500 (Illumina) was used to perform paired-end sequencing, generating 100 base reads. The average coverage of the exome for P4 and P5 was 97× and 86×, respectively. Sequence processing and mapping to the human reference genome assembly GRCh37 was performed with the Burrows-Wheeler Aligner, SAMtools, and Picard Tools. Variants were called by using the Genome Analysis Toolkit.

For all filtered variants, CADD PHRED scores, CADD_MSC, and pLi algorithms were used to assess the *in silico* predicted pathogenicity. *FCHO1* mutations were verified by means of Sanger sequencing in family members, and primer pairs are shown in Table E2.

Quantitative real-time PCR analysis

Normal donor PBMCs were stained and underwent fluorescence-activated cell sorting for surface expression of CD3 (eFluor450 mouse anti-human CD3, catalog #48003742, clone OKT3; Fisher Scientific, Waltham, Mass), CD4 (allophycocyanin [APC]–Cy7 mouse anti-human CD4 antibody, catalog #341095, clone SK3; BD Biosciences, San Jose, Calif), CD8 (PE mouse anti-human CD8 antibody, catalog #301008, clone RPA-T8; BioLegend, San Diego, Calif), CD19 (peridinin-chlorophyll-protein complex/Cy5.5 mouse anti-human CD19 antibody, catalog #302230, clone HIBI19; BioLegend), and

CD56 (fluorescein isothiocyanate [FITC] mouse anti-human CD56 antibody, catalog #340723, clone NCAM16.2; BD Biosciences), respectively, by using FACSAria. Total RNA was extracted from cells by using the RNeasy Micro Kit (Qiagen), according to the manufacturer's instructions. For each sample, cDNA was generated from RNA in a total volume of 20 mL by using the qScript cDNA Synthesis Kit (Quantabio, Beverly, Mass). Real-time PCR was performed with TaqMan Fast Advanced Master Mix (Applied Biosystems, Foster City, Calif) and TaqMan probes for human *ACTB* (Hs99999903_m1), *FCHO1* (Hs00322606_m1), and *FCHO2* (Hs01564786_m1; all from Thermo Fisher Scientific). Experiments were run on a 7500 Real Time PCR System (Applied Biosystems) with 7500 Real Time PCR software (version 2.3; Life Technologies, Grand Island, NY). Data were analyzed by using the $2^{-\Delta Ct}$ method after normalization to the *ACTB* gene as an endogenous control by using water as a negative control.

In vitro mutagenesis, transfection, and Western blotting

Targeted mutagenesis for mutations in P2 (c.2023dupG, p.V675Gfs*33) and P3 (c.1304_1305del, p.F436Wfs*7) was performed by using the Phusion Site-Directed Mutagenesis Kit (Thermo Fisher), according to the manufacturer's instructions. Wild-type (WT) cDNA of the human *FCHO1* gene from a pDONR-223 vector (Arizona State University) was introduced in an N-terminal tagged pCMV-HA-N vector (Addgene, Watertown, Mass), and the mutagenic primers FCHO1.P2 and FCHO1.P3 (see sequence below), which were designed by using the Phusion Site-Directed Mutagenesis Kit (Thermo Fisher) instructions, were used. Successful mutagenesis was confirmed my means of plasmid DNA sequencing at Macrogen (Seoul, Korea). One day before transfection, 293T cells were seeded (at 500,000 cells per well in a 6-well plate) in complete Dulbecco modified Eagle medium (DMEM/High Glucose from HyClone [San Angelo, Tex], 10% FBS from Gemini Bio-Products [West Sacramento, Calif], 1% MEM Non-Essential Amino Acid from Corning [Corning NY], and 1% L-glutamine from HyClone). Transfections were carried out with the Lipofectamine 3000 Transfection Kit (Invitrogen, Carlsbad, Calif), according to the manufacturer's protocol. Cells were transfected with 600 ng of FCHO1 WT, FCHO1.P2, or FCHO1.P3 plasmid DNA. After 24 hours, cells were harvested and used in immunoblotting. 293T transfected cells (10^6) were lysed with RIPA-NTG buffer (30 mmol/L Tris-Cl, 150 mmol/L NaCl, 1% NP-40, 1% Triton X-100, 10% glycerol, and 1× protease inhibitor) with protease inhibitor cocktail (Halt Protease Inhibitor Single-Use Cocktail 100×; Thermo Scientific) for 30 minutes on ice. Lysates were denaturated by using Bolt LDS Sample Buffer 4× and Bolt Reducing Agent 10× (Life Technologies) at 70°C for 15 minutes, loaded on 4-12% Bis-Tris Gel, and separated by using SDS-PAGE. Proteins were transferred to nitrocellulose membrane by using the iBlot 2 System (Invitrogen). Blots were probed overnight with 1:2000 dilutions of rat Anti-HA High Affinity mAb (11867423001; Roche, Mannheim, Germany), and 1:2000 dilution of rabbit anti–β-actin mAb (4967S; Cell Signaling, Danvers, Mass) as a loading control. Bands were revealed by using SuperSignal West Femto kit (Fisher Scientific).

For the mutation c.189dupC (P4), HEK293T cells were transfected with N-terminal FLAG-tagged FCHO1 WT (Genecopoeia, Rockville, Md) or FCHO1.P4 plasmid DNA. The latter was generated by using the QuikChange II XL Site-Directed Mutagenesis Kit (Agilent Technologies) with FCHO1.P4 primers (see sequence below). One day after transfection by using the TransIT-LT1 Transfection Reagent (Mirus Bio, Madison, Wis), cells were lysed in RIPA buffer (Millipore, Burlington, Mass), 50 mmol/L EDTA (Thermo Scientific), and protease inhibitors (Thermo Scientific). Electrophoresis of lysates was performed on 4-12% precast polyacrylamide gels (Invitrogen), followed by immunoblotting with the following antibodies as indicated in figure legends: anti-FLAG (F3165, Sigma-Aldrich, St Louis, Mo) and anti–β-actin (Sigma-Aldrich).

Primers for *in vitro* mutagenesis

FCHO1.P2 primer forward, CCACCACCACCTGGTCCTCAGCTTCCG; FCHO1.P2 primer reverse, GGTCCCGCTGAACACACGCACGATG; FCHO1.P3 primer forward, GTTCTTGGACACCTGCTCCTCTGACTGC; FCHO1.P3 primer reverse, CTTTGGGCCGCCCCTGGAGTCAGCCTTTG; FCHO1.P4 primer forward, CAGCAACGGGACCCCCCATGGGGAC; and FCHO1.P4 primer reverse GTCCCCATGGGGGGTCCCGTTGCTG.

Analysis of RNA splicing

RNA extracted from PBMCs derived from a healthy donor and from the father and mother of P1 was retrotranscribed with random primers and the ImProm-II Reverse Transcription System (Promega), according to the manufacturer's instructions. RT-PCR for *FCHO1* transcript was performed by using primers (forward, 5′TCTCCACAGAGACCATCAGG3′; reverse, 5′GATGCTGGACTCAGCCCTG3′) with an annealing temperature of 64°C.

In vitro T-cell activation and proliferation

For analysis of T-cell activation, PBMCs from P2 and 2 healthy control subjects were cultured in 200 μL of serum-supplemented RPMI (SH30027.01; GE Healthcare Life Sciences, Fairfield, Conn) in round-bottom 96-well plates with 1 μg/μL anti-CD3 (OKT3, catalog #14-0037-82; eBioscience, San Diego, Calif) and 1 μg/μL Protein A (catalog #P6031; Sigma-Aldrich) for 24 and 48 hours. Cells were collected at 24 and 48 hours, washed with serum-supplemented PBS, and stained with Live/Dead (L34959; Invitrogen) staining and fluorochrome-conjugated CD3-PE/Cy7 (317334; BioLegend), TCRαβ-FITC (555547; BD PharMingen), CD71-APC (17-0719-42; Invitrogen), CD69-BV510 (310936; BioLegend), and CD25-eFluor780 (47-0259-42; Invitrogen) for 15 minutes at 4°C (dark). On washing with serum-supplemented PBS, expression of CD69, CD25, and CD71 by $CD3^+$ cells was analyzed by using flow cytometry (LSRFortessa; BD) and FlowJo software (version 10.5.2; TreeStar, Ashland, Ore).

For analysis of T-cell proliferation, PBMCs were incubated with the CellTrace violet Cell Proliferation Kit (1 μmol/L; Invitrogen). After 20 minutes, 10 volumes of RPMI/10% FBS were added, and the cells were washed twice with RPMI/10% FBS. A total of 1 X 10^5 cells were seeded into 96-well plates and stimulated with Dynabeads CD3/CD28 (bead/cell ratio of 1:1; Invitrogen) for 4 days. Cells were then stained with fluorochrome-conjugated CD4 and CD8 antibodies (BD Biosciences) for 30 minutes at 4°C (dark) and washed twice with PBS twice, and CellTrace Violet expression was analyzed by using flow cytometry (Becton Dickinson FACSCanto II) and FlowJo software (version 10.5.2; TreeStar).

In vitro cell-cycle analysis

Total PBMCs were stimulated with Dynabeads Human T-Activator CD3/CD28 (Thermo Fisher) for 3 days. Cells were washed with PBS, fixed in 66% EtOH for 3 hours at 4°C, and then washed twice in PBS 2 times and stained with propidium iodide (50 μg/mL) for 30 minutes at 37°C in the presence of RNase A (100 μg/mL), followed by analysis with flow cytometry.

TCR internalization

PBMCs from P2 and 1 healthy control subject were either left unstimulated or stimulated with 0.5 μg/μL anti-CD3 (OKT3, catalog #14-0037-82; eBioscience) plus 0.5 μg/μL anti-CD28 (catalog #302914; BioLegend) in 500 μL of serum-supplemented RPMI at 37°C for 2, 15, and 30 minutes. At each time point, cells were collected, washed with serum-supplemented PBS, and stained with Live/Dead (L34959; Invitrogen) staining and fluorochrome-conjugated CD3-eFluor450 (48-0037-42; eBioscience) and TCRαβ-APC (17-9986-42; eBioscience) for 15 minutes at 4°C (dark). Cells were washed with serum-supplemented PBS, acquired, and analyzed by using flow cytometry (LSRFortessa; BD) and FlowJo software (version 10.5.2; TreeStar).

Transferrin internalization assay

PBMCs from P2 and 2 healthy control subjects were cultured in 200 μL of serum-supplemented RPMI (SH30027.01; GE Healthcare Life Sciences) in round-bottom 96-well plates with 1 μg/μL anti-CD3 (OKT3, catalog

#14-0037-82; eBioscience) and 1 μg/μL Protein A (catalog #P6031; Sigma-Aldrich) at 37°C for 48 and 72 hours. At each time point, cells were collected and washed with PBS at 300 relative centrifugal force units for 5 minutes and resuspended in 250 μL of RPMI serum-free media with 25 mmol/L HEPES (H3375-100G; Sigma) and 0.5% of BSA (15260-037; Life Technologies). Cells were starved for 30 minutes at 37°C, washed once with PBS, resuspended in serum-free RPMI with biotinylated transferrin (T23363; Invitrogen) and 0.5% BSA, and pulsed for 30 minutes at 4°C. Medium were then changed to serum-supplemented RPMI, and temperature was shifted to 37°C for 0, 10, and 30 minutes to stimulate biotinylated transferrin trafficking. Internalization was stopped by incubating cells on ice and washing with cold PBS, followed by staining and flow cytometry. For the different time point of transferrin internalization, the percentage of surface transferrin expression was calculated as follows:

$$\frac{\textit{Median fluorescence intensity (MFI) of surface transferrin at time } x}{\textit{MFI of surface transferrin at time } 0 \textit{ minutes}} \times 100.$$

Cells were the stained with Live/Dead (L34959; Invitrogen) staining and fluorochrome-conjugated CD3-PE/Cy7 (317334; BioLegend), TCRαβ-FITC (555547; BD PharMingen), and streptavidin-PE (554061; BD Biosciences) antibodies for 15 minutes at 4°C (dark) and then washed with serum-supplemented PBS twice analyzed by using flow cytometry (LSRFortessa; BD) and FlowJo software (version 10.5.2; TreeStar).

REFERENCES

E1. Paila U, Chapman BA, Kirchner R, Quinlan AR. GEMINI: integrative exploration of genetic variation and genome annotations. PLoS Comput Biol 2013;9:e1003153.

E2. Maffucci P, Bigio B, Rapaport F, Cobat A, Borghesi A, Lopez M, et al. Blacklisting variants common in private cohorts but not in public databases optimizes human exome analysis. Proc Natl Acad Sci U S A 2019;116:950-9.

E3. Erman B, Bilic I, Hirschmugl T, Salzer E, Boztug H, Sanal Ö, et al. Investigation of genetic defects in severe combined immunodeficiency patients from Turkey by targeted sequencing. Scand J Immunol 2017;85:227-34.

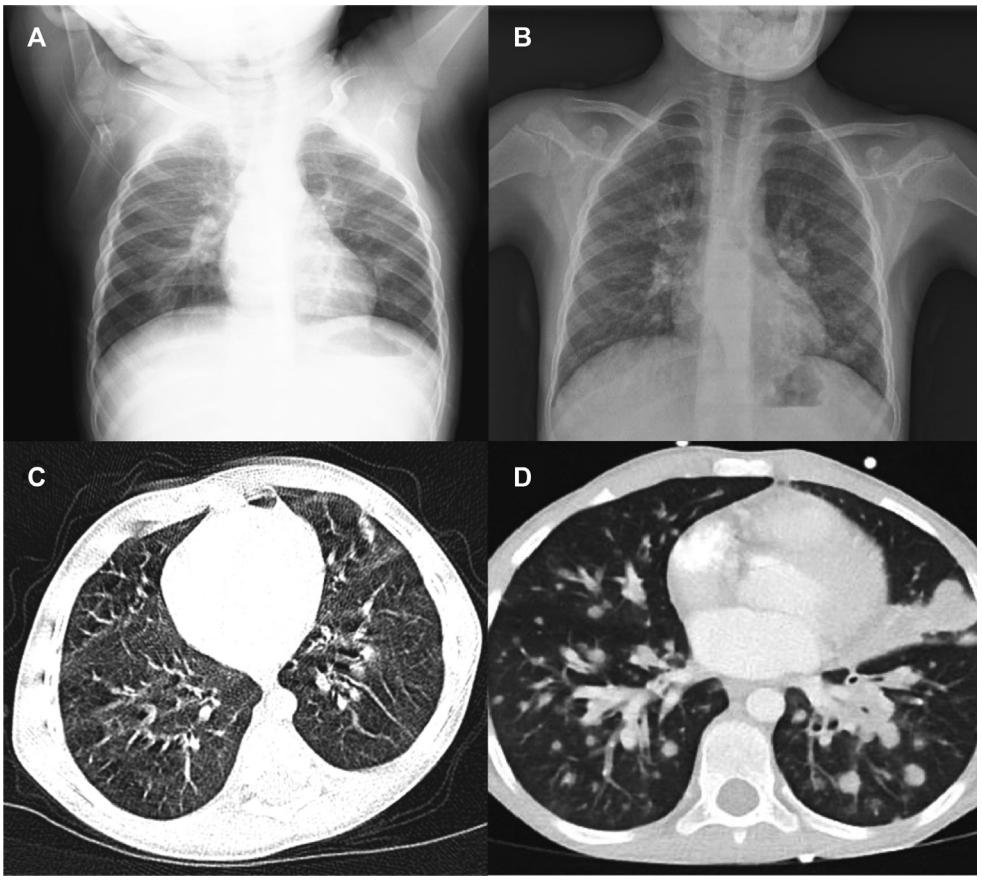


FIG E1. Anteroposterior chest radiography showing lack of thymic shadow in P2 **(A)** and P3 **(B)** and noncontrast chest CT scan showing bronchiectasis in P2 **(C)** and multiple parenchymal nodules in P3 **(D)**.

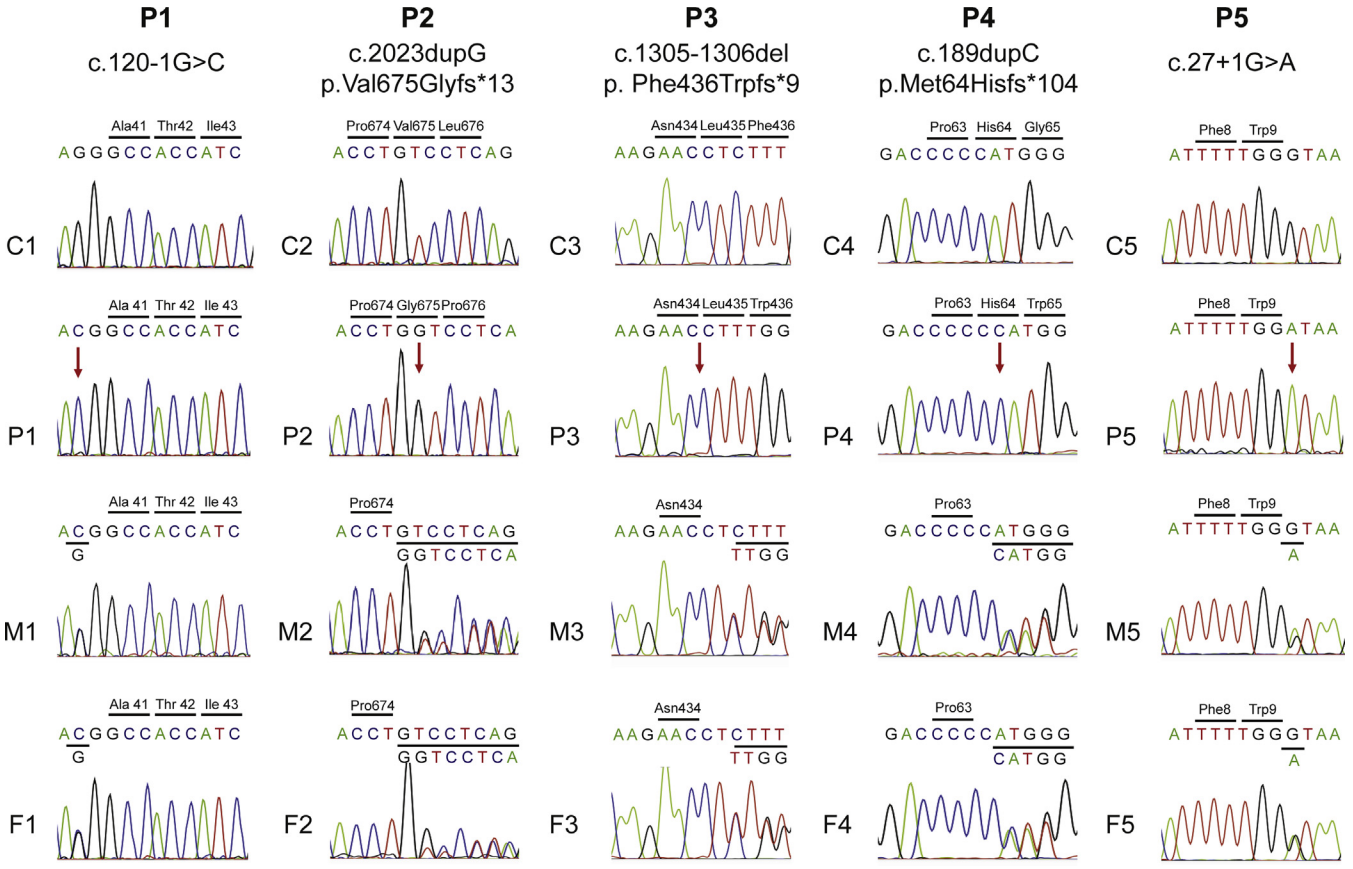


FIG E2. Chromatograms of *FCHO1* genomic DNA sequences in healthy control subjects (C1-C5), patients (P1-P5), and heterozygous carriers (mother, M1-M5; father, F1-F5) for each family. *Red arrows* indicate localization of homozygous mutations in the patients.

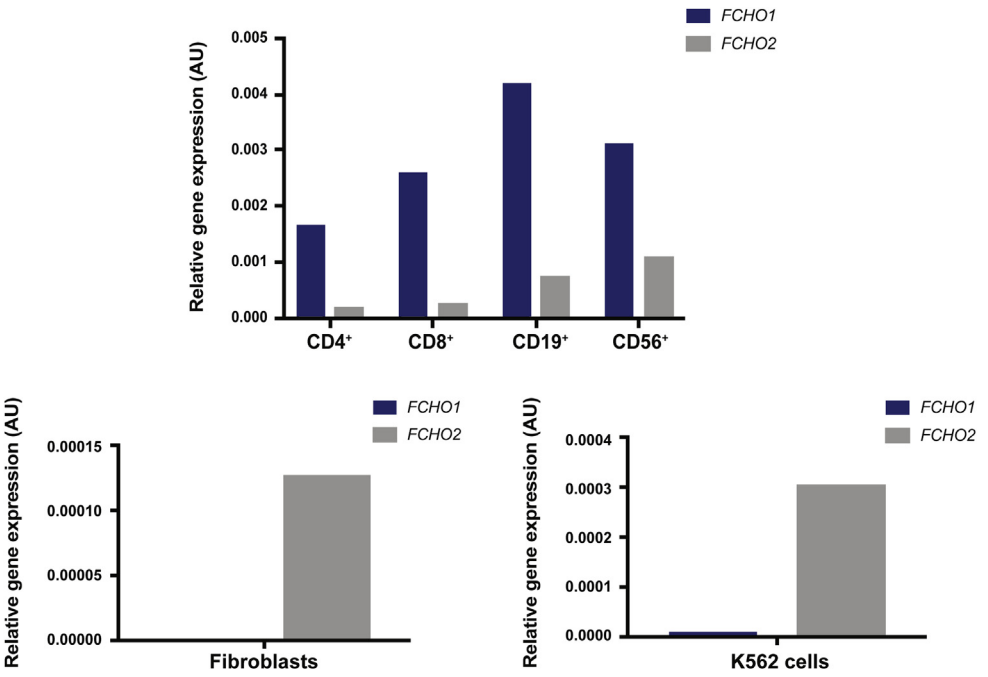


FIG E3. Relative expression of *FCHO1* and *FCHO2* transcripts in healthy donors' lymphoid subpopulations ($CD4^+$, $CD8^+$, $CD19^+$, and $CD56^+$ cells), fibroblasts, and K562 cells. Expression of target genes was normalized to β-actin reference gene expression levels within the same sample to determine Δ cycle threshold values.

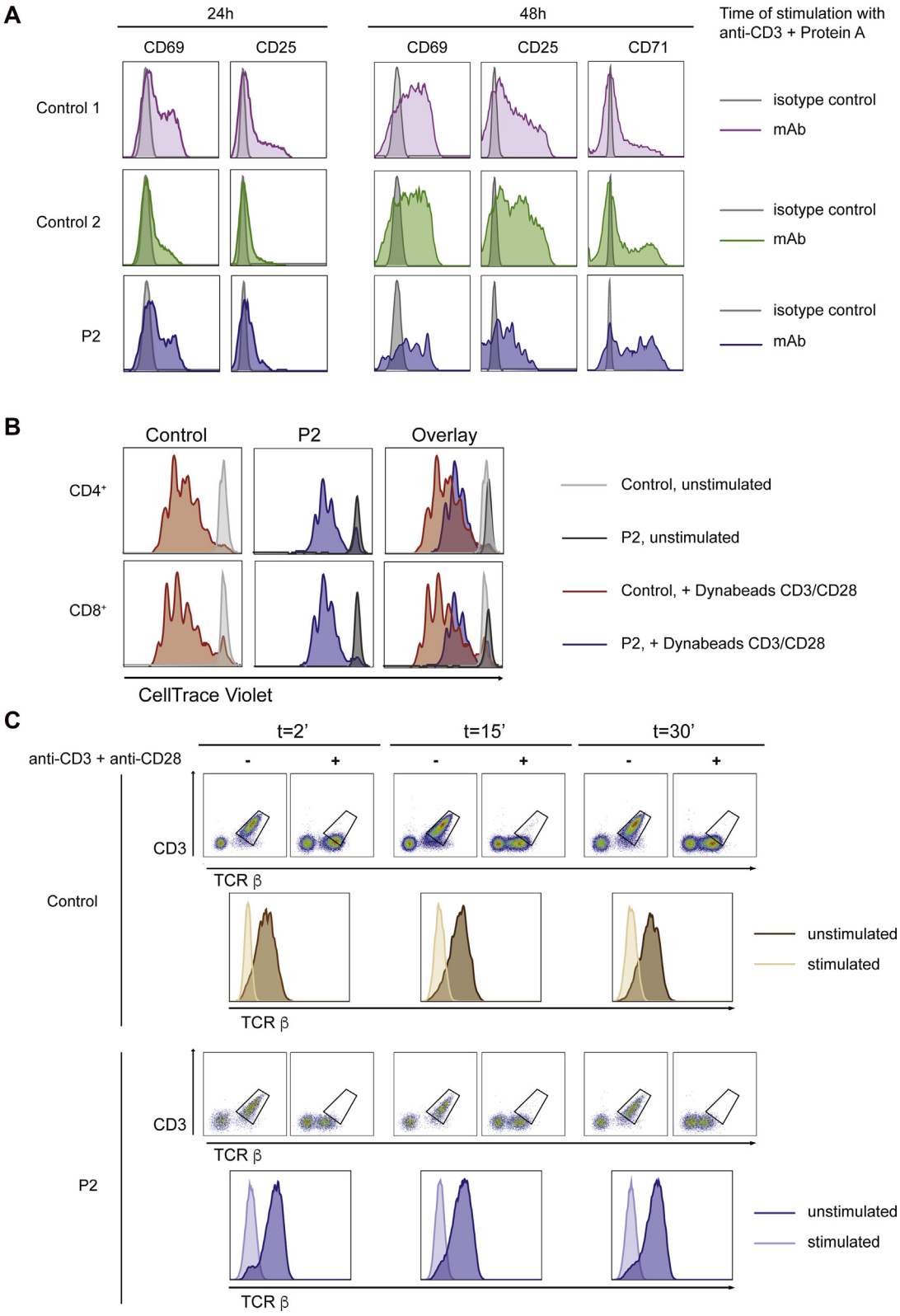


FIG E4. A, Surface expression of CD69, CD25, and CD71 after 24 and 48 hours of stimulation with anti-CD3 plus Protein A in T cells from 2 healthy control subjects and P2. Staining with isotype control is shown in gray. **B,** Dilution of CellTrace Violet staining as a readout of Dynabeads CD3/CD28-induced proliferation of $CD4^+$ *(top)* and $CD8^+$ *(bottom)* T cells from a healthy control subject *(left panels)* and P2 *(middle panels)*, with overlay shown in *right panels*. **C,** Flow cytometric analysis of the kinetics of TCRβ surface expression in unstimulated and anti-CD3/CD28–stimulated PBMCs from a healthy control subject *(upper panels)* and P2 *(lower panels)*.

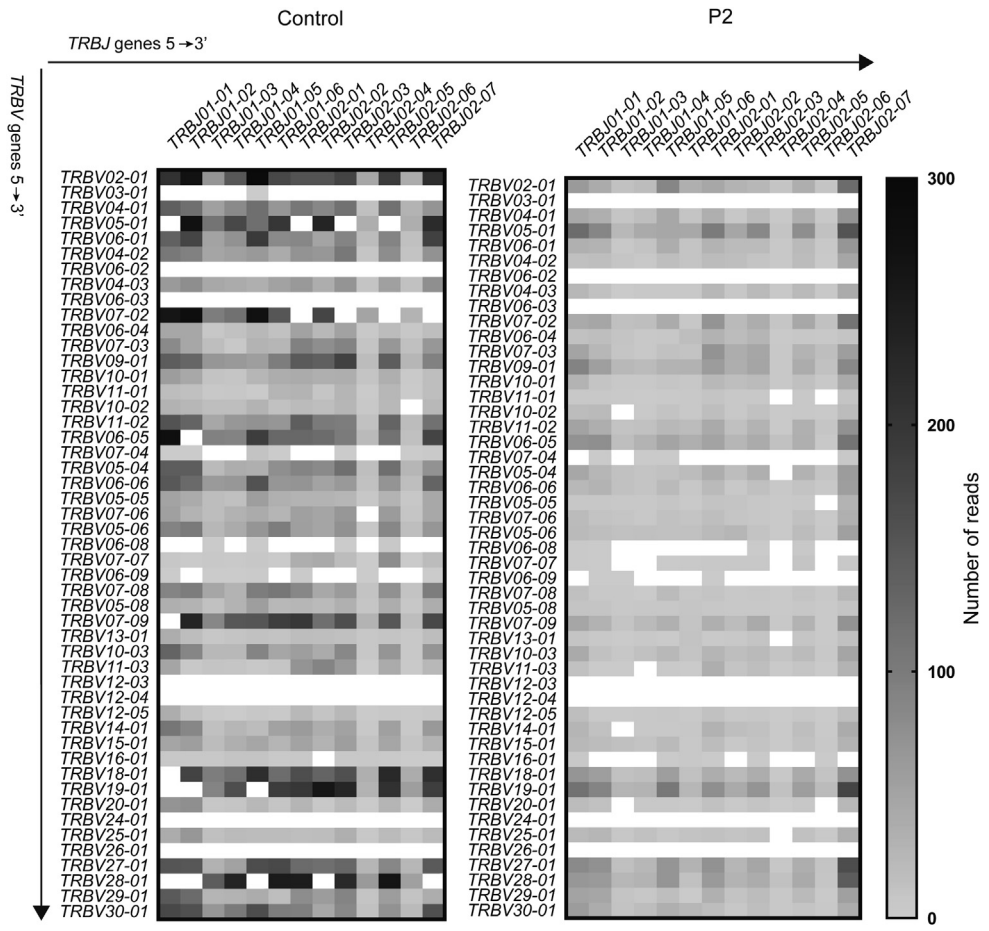


FIG E5. TCRβ *(TRB)* repertoire of peripheral blood T cells from a healthy control subject and P2. Shown is a heat map of *TRBV-TRBJ* gene productive rearrangements among total sequences obtained.

TABLE E1. Results of whole-exome sequencing and targeted sequencing of primary immune deficiency–related genes

Rare homozygous exonic and splice-site genetic variants identified in P1, P2, P4, and P5 by using whole-exome sequencing

	Gene	Type of variant	Transcript variant	Protein effect of the variant	EXAC MAF	gnomAD MAF	CADD PHRED score	CADD_MSC	pLi
P1	*FCHO1*	splice_acceptor_variant	NM_001161357.1:c.120-1G>C	NP_001093646:p.Asp4Val	—	—	26.3	5.744	1
	HOOK2	missense_variant	NM_001100176:c.11A>T	NP_006480:p.Pro256Ala	1.3E-04	1.1E-04	28.1	5.751	0
	NOVA1	missense_variant	NM_006489:c.766C>G	NP_001242941:p.Asp9Gly	8.2E-06	4.1E-06	24.3	3.313	0.98
	MYH10	missense_variant	NM_001256012:c.26A>G	NP_002552:p.Ala268Val	3.3E-05	2.2E-05	25.0	5.355	1
	P2RX5	missense_variant	NM_002561:c.803C>T	NP_056308:p.Arg662Gln	1.5E-04	1.6E-04	23.9	3.313	0
	KANK2	missense_variant	NM_015493:c.1985G>A		3.8E-04	4.0E-04	16.8	3.313	0.98
	SH3GLB2	splice_region_variant	NM_001287046:c.739-5C>T	NP_056093:p.Pro828Ser	4.8E-05	3.3E-05	13.0	5.263	0.37
	SASH1	missense_variant	NM_015278:c.2482C>T	NP_849188:p.Glu1324Gly	1.2E-03	1.2E-03	17.8	3.313	0
	RP1L1	missense_variant	NM_178857:c.3971A>G	NP_039228:p.Glu52Gln	—	—	0.0	0.009	0
	OR10H1	missense_variant	NM_013940:c.154G>C	NP_055861:p.Arg20His	8.7E-03	8.6E-03	9.5	3.313	0.64
	SETX	missense_variant	NM_015046:c.59G>A	NP_001156787:p.Ala130_Ala132del	9.1E-03	9.3E-03	0.2	0.006	0.2
	FBXL17	inframe_deletion	NM_001163315:c.388_396delGCT	NP_001078920:p.Ser93_His94ins	2.1E-03	8.2E-04	12.0	5.778	0.98
	LNP1	inframe_insertion	GCCGCC	SerAspArgLeuProArgArgHisSerHis	—	—	4.2	3.313	0
	NOP9	inframe_insertion	NM_001085451:c.260_261insGGAA TTCCGATGCCGATCGTCTGACC GTCTTCCTAGAAGGCATTCTCA TGAGGACCA NM_001286367:c.504_509dupGGAGGA	GluAspGlnGluPheArgCysArgSer NP_001273296:p.Glu168_Glu169dup	—	—	10.8	3.313	0
P2	*FCHO1*	frameshift_variant	NM_001161357.1:c.2023dupG	NP_001154829.1:p.Val675Glyfs*13	—	—	34.0	5.744	1
	ZNF730	frameshift_variant	NM_001277403:c.906dupT	NP_001264332:p.Lys303*	3.9E-03	3.6E-03	23.3	3.313	0
	MEGF9	missense_variant	NM_001080497:c.502A>G	NP_001073966:p.Thr168Ala	2.0E-03	1.9E-03	16.1	3.313	0.92
	AKAP8	missense_variant	NM_005858:c.676G>A	NP_005849:p.Glu226Lys	3.0E-03	2.5E-03	24.4	3.313	0.98
	KIAA0947	missense_variant	NM_015325:c.4610C>G	NP_056140:p.Ser1537Cys	—	—	23.2	3.313	1
	SV2C	splice_region_variant	NM_001297716:c.1137+3G>T		6.6E-05	6.1E-05	22.0	3.313	0
	GALR3	missense_variant	NM_003614:c.935G>T	NP_003605:p.Arg312Leu	8.0E-04	1.4E-03	15.8	5.745	0.02
	FAM105B	missense_variant	NM_138348:c.345G>T	NP_612357:p.Gln115His	6.5E-03	6.6E-03	15.7	3.313	0.97
	AP3B1	missense_variant	NM_003664:c.2995G>A	NP_003655:p.Val999Met	3.8E-03	4.1E-03	14.0	0.879	1
	TRIO	missense_variant	NM_007118:c.7292A>C	NP_009049:p.Asp2431Ala	—	—	16.8	3.313	1
	MAP1S	missense_variant	NM_001308363:c.1831C>T	NP_001295292:p.Arg611Cys	4.2E-04	2.0E-04	13.4	3.313	0.64
	CSDC2	splice_region_variant	NM_014460:c.300-6C>T		2.8E-03	2.8E-03	5.0	5.764	0.08
	PCNT	missense_variant	NM_006031:c.5771C>T	NP_006022:p.Ala1924Val	7.4E-03	6.0E-03	0.5	0.001	0

(Continued)

TABLE E1. *(Continued)*

Rare homozygous exonic and splice-site genetic variants identified in P1, P2, P4, and P5 by using whole-exome sequencing

	Gene	Type of variant	Transcript variant	Protein effect of the variant	EXAC MAF	gnomAD MAF	CADD PHRED score	CADD_MSC	pLi
P4	*FCHO1*	frameshift_variant	NM_001161357.1:c.184_185insC	NP_001154829.1:p.Met64Hisfs*104	8.2E-06	—	28.9	5.744	1
	AIM1L	disruptive_inframe_deletion		NP_001034864.2:p.Asp539_	7.1E-05	—	2.4	5.798	0
	KIAA0040	missense_variant	NM_001039775.3:c.1593_1643delC	Pro555del	—	—	14.8	10.903	0
	THADA	missense_variant	GTGAAGGGCCCCGGTGCTCCTG	NP_055471.2:p.Asn65Lys	4.4E-05	3.0E-05	10.3	3.313	0
	CAND2	splice_acceptor_variant	ATGCCTCATTTCCCACCTGGAA	NP_071348.3:p.His1663Gln	—	—	32.0	3.313	0
	MUC4	missense_variant	AGAGGT		—	1.6E-03	7.6	3.313	0
	ZNF718	missense_variant	NM_014656.2:c.195C>A	NP_060876.5:p.Ala1198Thr	2.2E-03	2.4E-03	3.3		NA
	DGKQ	missense_variant	NM_022065.4:c.4989C>G	NP_001034216.2:p.Asn317=	9.5E-04	1.7E-03	19.3	3.313	0
	DGKQ	splice_region_variant	NM_001162499.1:c.492-1G>A	NP_001338.2:p.Arg240His	—	—	9.9	3.313	0
	GRK4	frameshift_variant	NM_018406.6:c.3592G>A		4.9E-04	5.2E-04	31.0	3.313	0
	HTT	splice_region_variant	NM_001039127.5:c.951T>C	NP_892027.2:p.Arg222Lysfs	8.2E-04	7.9E-04	8.6	3.313	1
	ADH1B	missense_variant	NM_001347.3:c.719G>A		8.2E-05	8.9E-05	24.5	3.313	0.19
	MTTP	missense_variant	NM_001347.3:c.272-3C>T	NP_000659.2:p.Arg313Cys	2.3E-04	3.5E-04	15.5	0.002	0.01
	TXNDC5	missense_variant	NM_182982.2:c.655_656insA	NP_001287714.1:p.Pro913Leu	—	3.3E-04	12.3	3.313	0
	KLHL31	missense_variant	NM_002111.8:c.529-3C>T	NP_110437.2:p.Arg37Gln	2.0E-03	2.3E-03	26.1	3.313	0.02
	ZP3	splice_region_variant	NM_000668.5:c.937C>T	NP_001003760.2:p.Val111Met	6.9E-04	7.5E-04	0.6	3.313	0
	FBXW8	missense_variant	NM_001300785.1:c.2738C>T		—	0.0E+00	23.9	3.313	0
	DZIP1	missense_variant	NM_030810.4:c.110G>A	NP_699179.2:p.His294Asp	3.1E-04	3.4E-04	24.4	3.313	0
	GOLGA6L2	missense_variant	NM_001003760.4:c.331G>A	NP_945319.1:p.Pro657Leu	9.6E-05	—	11.4	3.313	0
	DENND4A	missense_variant	NM_001110354.1:c.536-4T>A	NP_001291317.1:p.Ala806Pro	—	—	16.3	3.313	0
	ZFPM1	disruptive_inframe_deletion	NM_153348.2:c.880C>G	NP_001307764.1:p.Ser1315Gly	1.4E-03	1.2E-03	10.2	3.313	0.03
	WRAP53	missense_variant	NM_198968.3:c.1970C>T	NP_722520.2:p.Leu446_Ala447del	4.1E-04	3.5E-04	7.7	23.7	0.62
	USP22	missense_variant	NM_001304388.1:c.2416G>C	NP_060551.2:p.Val63Met	1.7E-05	8.1E-06	24.7	5.562	0.98
	ECSIT	missense_variant	NM_001320835.1:c.3943A>G	NP_056091.1:p.Leu205Met	—	4.1E-06	0.1	3.313	0.02
	RFX1	missense_variant	NM_153813.2:c.1334_	NP_057665.2:p.Ser49Ile	2.5E-05	4.5E-05	26.1	3.313	1
	NOTCH3	missense_variant	1339delCTCTGG	NP_002909.4:p.Gln280Arg	1.6E-04	2.3E-04	28.7	12.19	0.21
			NM_018081.2:c.187G>A	NP_000426.2:p.Val2021Met					
			NM_015276.1:c.613C>A						
			NM_016581.4:c.146G>T						
			NM_002918.4:c.839A>G						
			NM_000435.2:c.6061G>A						

(Continued)

TABLE E1. *(Continued)*

	Gene	Type of variant	Transcript variant	Protein effect of the variant	EXAC MAF	gnomAD MAF	CADD PHRED score	CADD_MSC	pLi
Rare homozygous exonic and splice-site genetic variants identified in P1, P2, P4, and P5 by using whole-exome sequencing									
P5	*FCHO1*	splice_donor_variant	NM_001161357.1:c.27+1G>A		—	—	33.0	5.744	1
	PTCD3	missense_variant	NM_017952.5:c.1028G>A	NP_060422.4:p.Arg343Gln	3.3E-05	4.5E-05	26.2	3.313	0
	NIFK	frameshift_variant	NM_032390.4:c.683_684delTG	NP_115766.3:p.Val228Glyfs	—	—	24.3	3.313	0
	ARPP21	missense_variant	NM_001267619.1:c.1871C>T	NP_001254548.1:p.Ser624Leu	—	—	23.4	3.313	0
	XIRP1	missense_variant	NM_194293.2:c.4991G>A	NP_919269.2:p.Arg1664Gln	2.9E-04	3.9E-04	16.7	3.313	0
	TOPAZ1	missense_variant	NM_001145030.1:c.4783A>G	NP_001138502.1:p.Ile1595Val	2.8E-03	1.7E-03	22.6	3.313	0.99
	DNAH1	missense_variant	NM_015512.4:c.888G>C	NP_056327.4:p.Gln296His	6.5E-04	6.6E-04	8.9	22.1	0
	PRKCD	missense_variant	NM_006254.3:c.1928G>A	NP_006245.2:p.Arg643His	9.9E-05	1.1E-04	23.8	26.5	1
	CFAP44	missense_variant	NM_001164496.1:c.5396G>A	NP_001157968.1:p.Arg1799Gln	—	2.8E-05	23.4		0
	ZNF595	splice_acceptor_variant	NM_182524.3:c.634+2C>T		—	—	0.4	4.487	0
	MAST4	missense_variant	NM_001164664.1:c.6014C>G	NP_001158136.1:p.Thr2005Ser	1.5E-04	1.7E-04	6.9	3.313	0.01
	C5orf63	missense_variant	NM_001164479.1:c.37A>G	NP_001157951.1:p.Arg13Gly	4.3E-05	5.0E-05	22.9		0
	AP5Z1	missense_variant	NM_014855.2:c.1162G>A	NP_055670.1:p.Val388Ile	5.8E-05	5.7E-05	10.6	23.8	0
	RADIL	missense_variant	NM_018059.4:c.1142T>C	NP_060529.4:p.Leu381Pro	—	—	16.4	3.313	0
	SKAP2	missense_variant	NM_003930.4:c.583C>A	NP_003921.2:p.Arg195Ser	—	—	31.0	8.906	0.91
	GARS	missense_variant	NM_002047.3:c.269A>G	NP_002038.2:p.Asp90Gly	8.3E-06	4.1E-06	24.7	22.9	0.79
	CDK13	missense_variant	NM_003718.4:c.4247C>A	NP_003709.3:p.Pro1416His	9.1E-05	5.7E-05	26.6	3.313	0.75
	MAMDC4	splice_region_variant	NM_206920.2:c.796+7C>T		—	—	10.9	3.313	0
	ANAPC2	missense_variant	NM_013366.3:c.522G>C	NP_037498.1:p.Gln174His	8.2E-06	—	20.7	3.313	0.99
	KMT2D	missense_variant	NM_003482.3:c.8669C>G	NP_003473.3:p.Pro2890Arg	—	1.2E-05	25.0	0.001	1
	RGS11	missense_variant	NM_183337.2:c.647G>A	NP_899180.1:p.Arg216His	2.8E-05	3.8E-05	0.5	3.313	0
	TMEM8A	missense_variant	NM_021259.2:c.1139C>T	NP_067082.2:p.Ser380Leu	3.7E-04	3.5E-04	14.6	3.313	0
	FTSJ3	missense_variant	NM_017647.3:c.485G>A	NP_060117.3:p.Arg162His	8.2E-06	8.1E-06	27.3	3.313	0.48
	GNA13	missense_variant	NM_006572.5:c.445A>G	NP_006563.2:p.Ile149Val	2.5E-04	2.6E-04	23.7	5.785	0.53
	AXIN2	missense_variant	NM_004655.3:c.986G>A	NP_004646.3:p.Ser329Asn	1.6E-05	1.6E-05	23.1	21.7	0.12
	RNF213	splice_region_variant	NM_001256071.2:c.11972+8C>T		3.2E-03	3.6E-03	3.1	3.313	0
	MYO1F	missense_variant	NM_012335.3:c.943G>A	NP_036467.2:p.Gly315Arg	1.7E-04	1.7E-04	16.2	3.313	0.16
	F2RL3	missense_variant	NM_003950.3:c.554G>A	NP_003941.2:p.Arg185His	—	9.4E-06	24.1	3.313	0
	PCNT	missense_variant	NM_006031.5:c.7252G>A	NP_006022.3:p.Gly2418Ser	2.5E-05	3.3E-05	12.8	0.001	0
Variants identified on targeting sequencing of >500 immune-related genes									
P3	Homozygous variants								
	FCHO1	frameshift_variant	NM_001161357.1:c.1305_1306del	NP_001154829.1:p.Phe436Trpfs*9	—	—	33.0	4.74	1
	Heterozygous variants								
	C1QB	splice_acceptor_variant	NM_000491:c188-1G>T		—	—	32.0	19.64	0.16
	CCDC40	missense_variant	NM_001243342.1:c.2891A>G	NP_000482.3:p.His964Arg	—	8.9E-02	4.3	0	0
	EMR2	missense_variant	NM_013447.4:c.185C>T	NP_038475.2:p.Met62Thr	1.5E-04	3.2E-05	1.2	2.31	0
	IL17F	missense_variant	NM_052872.3:c.230G>A	NP_443104.1:Arg77His	5.8E-05	4.5E-05	26.2	2.31	0.04
	PARN	missense_variant	NM_002582.4:c.1785T>G	NP_002573.1: Asp595Glu	2.3E-04	2.1E-04	5.7	2.31	0
	TNFAIP3	missense_variant	NM_006290.3:c.1189T>C	NP_001257436.1:Ser397Pro	—	—	28.3	2.31	1

MAF, Minor allele frequency; *NA*, not applicable.

TABLE E2. Sequence of primers used for Sanger confirmation of *FCHO1* mutations

Patient	Primer	Sequence (5′–3′)
P1	Forward amplification	CCTAACCTCAGGTGATCCGT
	Reverse amplification	CCATAATCGAGGTGGATGAC
	Forward sequencing	CCTAACCTCAGGTGATCCGT
	Reverse sequencing	CCATAATCGAGGTGGATGAC
P2	Forward amplification	AGGCACCAGTGAAACCAAGA
	Reverse amplification	CCCAGGAAGCAGAGAGGGAA
	Forward sequencing	AGGCACCAGTGAAACCAAGA
	Reverse sequencing	CCCAGGAAGCAGAGAGGGAA
P3	Forward amplification	GGATGAGGCTTGGGAAAAAT
	Reverse amplification	CCTCATTGGCCTAACTCTGC
	Forward sequencing	GGATGAGGCTTGGGAAAAAT
	Reverse sequencing	CCTCATTGGCCTAACTCTGC
P4	Forward amplification	CCACTGCTAAGGTGTTTGAG
	Reverse amplification	TTAACATCTCTCTTCTCACACAG
	Forward sequencing	TCCATCTTTACCTCATTCTCCT
	Reverse sequencing	ATCCAAATAGCCCCATAATCG
P5	Forward amplification	GCTATGAACTCTTATACATGCCTAAA
	Reverse amplification	AATGAATGAATAAAAACAACTCTGTC
	Forward sequencing	AAACTTGCCTCTCTCTTCAGA
	Reverse sequencing	TGACTCTTCCCACTTTAACTTC